Enhanced Electron Collection Efficiency in Dye-Sensitized Solar Cells Based on Nanostructured TiO$_2$ Hollow Fibers

Elham Ghadiri,[†] Nima Taghavinia,*[,†,‡] Shaik M. Zakeeruddin,[§] Michael Grätzel,[§] and Jacques-E. Moser*[,§]

[†]Institute for Nanoscience and Nanotechnology and [‡]Physics Department, Sharif University of Technology, Tehran 14588, Iran and [§]Institute of Chemical Sciences and Engineering, Ecole Polytechnique Fédérale de Lausanne, CH-1015 Lausanne, Switzerland

ABSTRACT Nanostructured TiO$_2$ hollow fibers have been prepared using natural cellulose fibers as a template. This cheap and easily processed material was used to produce highly porous photoanodes incorporated in dye-sensitized solar cells and exhibited remarkably enhanced electron transport properties compared to mesoscopic films made of spherical nanoparticles. Photoinjected electron lifetime, in particular, was multiplied by 3−4 in the fiber morphology, while the electron transport rate within the fibrous photoanode was doubled. A nearly quantitative absorbed photon-to-electrical current conversion yield exceeding 95 % was achieved upon excitation at 550 nm and a photovoltaic power conversion efficiency of 7.2 % reached under simulated AM 1.5 (100 mW cm^{-2}) solar illumination.

KEYWORDS Dye-sensitized solar cells, TiO$_2$ nanostructured hollow fibers, charge transport, interfacial electron transfer dynamics, transient photovoltage and photocurrent, time-resolved diffuse reflectance

Dye-sensitized nanocrystalline solar cells (DSC) are of great interest as a cost-effective alternative to conventional silicon photovoltaics.[1,2] The photoanode in DSC is a mesoporous anatase TiO$_2$ film consisting of interconnected spherical nanoparticles, sensitized by a monolayer of dye molecules. Upon visible light absorption, excited sensitizer molecules inject an electron into the conduction band of TiO$_2$. These carriers are subsequently transported toward and collected by a back-contact electrode. Typical 10 μm thick mesoporous films made of 20 nm diameter particles are characterized by a roughness factor exceeding 1000. Despite the moderate extinction coefficient of Ru(II) polypyridyl dyes used as sensitizers, the large surface area of the nanocrystalline semiconductor allows for the adsorption of enough dye molecules to ensure practically quantitative harvesting of solar light at wavelengths shorter than 600 nm. The use of a light-scattering layer, made of larger TiO$_2$ particles deposited on top of the mesoporous film, further increases the radiation path length within the film and improves in particular the harvesting of red photons.[3] Further optimization of the photovoltaic performances of the device can be achieved by adjusting the composition of the electrolyte. A certified overall power conversion efficiency of up to $\eta = 11.1$ % has been achieved so far by optimal devices under AM 1.5 solar illumination.[4] Dye-sensitized solar cells based on similar TiO$_2$ mesoporous films deprived from the large particle light-scattering layer typically exhibit efficiencies of the order of $\eta = 7-8$ %.

Transport of photoinjected electrons in the oxide network to the back contact is believed to occur by diffusion and to be strongly limited by trapping and detrapping within particles and at grain boundaries.[5,6] This slow electron transport process competes with recombination of carriers with the electrolyte at the surface. The limitation imposed on the electron transport by the mesoporous structure hinders the progress in achieving higher conversion efficiencies. Apparent electron diffusion coefficients, D_n*, and dynamic electron lifetimes, τ_n, in the solid have been shown to predict well the photovoltaic performance of the DSC. Indeed, a majority of photogenerated carriers are collected when the effective diffusion length, L_n, of electrons is larger than the film thickness, d: $L_n = (D_n*/\tau_n)^{1/2} > d$.[7] An alternate TiO$_2$ film morphology with improved charge collection efficiency would imply that the trapping of electrons by structural defects such as interparticle connections is minimized, increasing the electron diffusion path length.

One-dimensional nanostructures, such as tubes, wires, and fibers, have recently attracted much attention in research dealing with new morphologies of TiO$_2$ photoactive layers in DSCs.[8-15] In addition to the potential of improving of electron transport, these nanomaterials provide a large surface area for the adsorption of the dye and also enhance light harvesting efficiency by scattering more light in the red part of the solar spectrum, where the absorption of currently used molecular sensitizers is weak. Among these systems, TiO$_{(2)}$ nanotube arrays grown perpendicular to the anode substrate gave so far the best results.[16-18] This particular

material architecture apparently offers reduced trapping of photoinjected electrons during their path to the back contact. Concomitantly, the redox mediator is expected to diffuse faster in the straight pores and thus transport positive charges more readily than in the tortuous structure characterizing mesoporous layers. DSCs based on vertically aligned nanotubes prepared by anodization of Ti metal, however, suffer generally from a rather low surface area. With an acetonitrile solvent-based electrolyte, a maximum power conversion efficiency of $\eta = 6.9\%$ was recently reached with this TiO_2 photoanode morphology.[18]

Here we report on the preparation of TiO_2 fibers via a template-based method. Thus obtained hollow microfibers were characterized by a nanostructured, porous surface. They were cast in the form of highly scattering films and used as a photonanode in DSC. When sensitized by a high extinction coefficient Ru(II) complex dye and using a standard (I_3^-/I^-) redox mediator-based electrolyte, these systems achieved excellent power conversion efficiencies reaching $\eta = 7.2\%$ under simulated AM 1.5 sunlight irradiation. In similar conditions, where no large particles light scattering layer was used, the photovoltaic performance of devices based on standard layers consisting of spherical nanoparticles was very much comparable, with $\eta = 7.3\%$. Electron transport was scrutinized in both titania fibers and spherical nanoparticle morphologies using transient photovoltage technique. Also, nanosecond transient optical diffuse reflectance spectrometry was applied to opaque fibrous layers to monitor the dynamics of the oxidized dye species at the surface. Results converge in showing a remarkable enhancement of the electron transport efficiency for fibers compared to sintered spherical particle layers, and a near 100% internal conversion quantum yield for electric current generation.

TiO_2 fibers were prepared using cellulose fibers as a template. Cellulose is the most abundant natural polymer. In the form of cotton wool wadding it consists of fibers of a few micrometers in diameter and of typically hundred micrometers length, with a surface area of about 1 m^2/g. It is low cost, ecological, and economically favored for practical applications. Figure 1 schematizes the preparation steps of TiO_2 nanostructured fibers. In a typical synthesis, supersaturated aqueous solutions of $(NH_4)_2TiF_6$ (Aldrich) and H_3BO_3 (Merck) at 50 °C were used to deposit TiO_2 on cotton fibers (Flawa, oxygen-bleached, hydrophilic, 100% pure cotton wool). Concentration of the Ti(IV) precursor and the pH of the solution were adjusted to 0.03 M and 2.0, respectively. In such conditions, the solution supersaturation is low and stepwise hydrolysis and dehydration of $(NH_4)_2TiF_6$ produces TiO_2 nanoparticulate films on hydrophilic cellulose fibers through heterogeneous nucleation. The dependence of the conditions of supersaturated solution and the morphology of resultant TiO_2 fibers upon synthesis parameters, such as the $(NH_4)_2TiF_6$ concentration, the pH of the solution and the deposition time, was scrutinized and these results will be
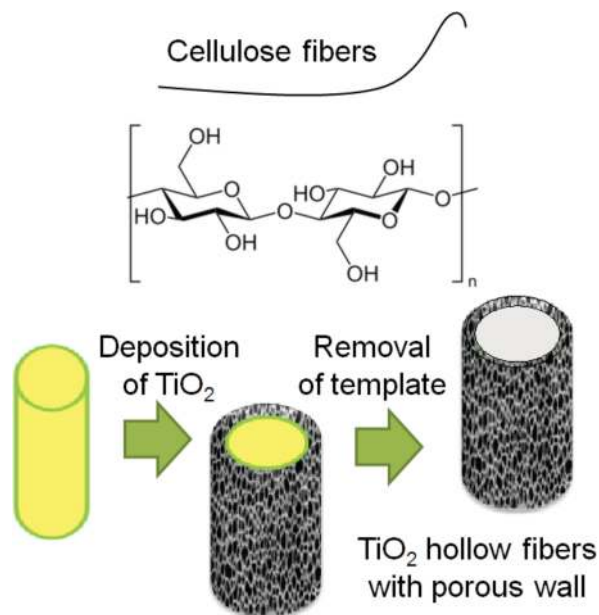

FIGURE 1. Scheme of TiO_2 fiber preparation steps.

published elsewhere. After deposition of TiO_2 on fibers for 5 h, these were washed with deionized water and dried overnight. The cellulose template was removed by heating the samples at 500 °C in air for 3 h. Following this recipe all organic material was burnt out and pure TiO_2 fibers remained as a result, without significant cross-linking. The morphological aspects of samples and the crystallinity of titania were characterized by scanning electron microscopy (SEM, Phillips XL30) and X-ray powder diffraction (XRD, Bruker, D4 Endeavor) techniques. The specific surface area of TiO_2 fibers was determined by BET adsorption−desorption experiments (Belsorp mini II). The measured value of 52 m^2/g was much larger than that obtained for the cellulose template (1 m^2/g). It implies that the surface of titania hollow fibers is highly nanostructured and offers additional porosity that will be essential for the loading of dye sensitizer molecules.

Nanocrystalline films used to constitute the DSC photoanode were cast on transparent conducting glass using the doctor-blade method. A dispersion of 15 wt % of TiO_2 fibers in water was acidified by 10^{-3} M HNO_3 and lightly milled in a mortar. After 1 h of stirring, the dispersion was treated with a 40 W ultrasonic titanium probe at a frequency of 15 pulses/s followed by addition of hydroxypropyl cellulose (HPC, MW 20000) at a rate of 20% (by wt) with respect to TiO_2 content and further stirring. The obtained TiO_2 paste was doctor-bladed with an automatic moving blade. Prior and after TiO_2 coating, the sample was treated with a 40 mM $TiCl_4$ aqueous solution for 30 min at 70 °C. Finally the titania paste film was heated at 470 °C in air for approximately 30 min. During this process, the HPC was burnt out and the nanostructured fibers cross-linked together by sintering, yielding a mechanically resistant and opaque film, whose thickness could easily be adjusted from $d = 2$ to 10 μm.
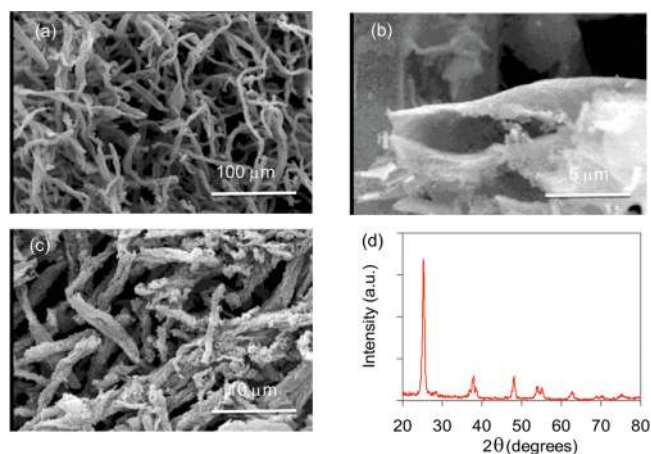
FIGURE 2. (a) SEM micrograph of TiO$_2$ fibers just after the organic template was removed by heat treatment. (b) SEM image showing the cross section of one hollow fiber. (c) Typical SEM image of TiO$_2$ nanofibers obtained after milling and ultrasonication to make a paste. (d) XRD diagrams of the TiO$_2$ fibers.

FIGURE 3. Absorptance spectrum (α) calculated from measured diffuse reflectance (R_d) and diffuse transmittance (T_d) spectra of a C101 dye-sensitized, 6 μm thick film made of TiO$_2$ fibers. The IPCE photocurrent action spectrum was recorded for DSCs based on similar dye-sensitized 6 μm thick films. The absorbed photon-to-current conversion efficiency (APCE = IPCE/α) data were finally extracted from the two latter spectra.

Scanning electron microscopy (SEM) images of TiO$_2$ microfibers are shown in Figure 2. After initial heat treatment of template-coated fibers, the cellulose was removed yielding 100 μm long TiO$_2$ hollow fibers (Figure 2a). A diameter of 1−2 μm was estimated for these fibers. The open-end tubular structure of one fiber can be observed in Figure 2b. Figure 2c shows a SEM picture of fibers after they underwent milling and ultrasonication. The latter processes applied during the preparation of the TiO$_2$ paste apparently broke a majority of the fibers to a length of approximately 10−20 μm. Figure 2d shows the X-ray diffraction pattern of the fibers. All the peaks in the XRD pattern can be ascribed to polycrystalline anatase TiO$_2$. Using the Scherrer equation, the average crystalline domain size was estimated to be 11 nm, which is consistent with the nanostructure of the fibers' surface inferred from BET measurements.

Sintered TiO$_2$ fibrous films deposited on conductive glass (NSG10, sheet resistance 10 Ω sq^{-1}) were dyed by dipping in 0.3 mM solutions in acetonitrile of the ruthenium complex Na−Ru^{II}(4,4′-bis(5-hexylthiophen-2-yl)-2,2′-bipyridine)(4-carboxylic acid-4′-carboxylate-2,2′-bipyridine)(NCS)$_2$ (C101).[4] This heteroleptic polypyridyl ruthenium(II) complex benefits from enhanced π-conjugation of the spectator (noncarboxylated) ligand and is characterized by a high molecular extinction coefficient. In conjunction with an acetonitrile-based electrolyte, it has reached already a strikingly high conversion efficiency of $\eta \geq 11.0\%$.[4] Test solar cells were then prepared according to a previously described procedure.[3] The redox-active electrolyte (coded Z960) used throughout the present study consisted of 1.0 M 1,3-dimethylimidazolium iodide, 0.05 M LiI, 0.1 M guanidinium thiocyanate, 0.03 M I$_2$, and 0.5 M tert-butylpyridine in a solvent mixture of acetonitrile and valeronitrile (85/15, v/v).

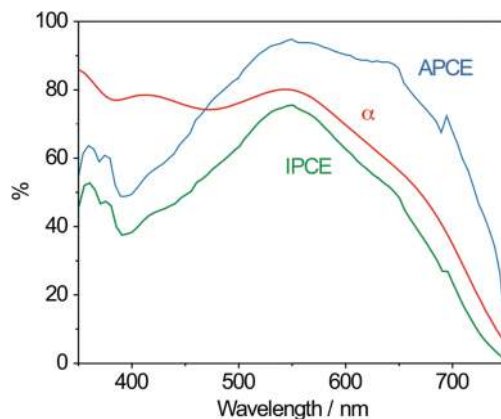Dye loading on the surface of TiO$_2$ was quantified by desorbing the dye from the electrode surface in alkaline aqueous medium. The amount of dye adsorbed within 6 μm thick films made of fibers and spherical nanoparticles was 5.0 × 10^{-8} and 7.1 × 10^{-8} mol/cm^2, respectively, with regard to the macroscopic geometric area of the TiO$_2$ electrode. Assuming a monolayer dye coverage of 1.04 × 10^{-10} mol/cm^2, the roughness factor of 6 μm thick fibrous films was estimated to be $\rho = 470$ and, thus, approximately 30% inferior to that of mesoporous particulate layers of identical thickness, for which a value of $\rho = 680$ was calculated. Visible diffuse reflectance (R_d) and diffuse transmittance (T_d) spectra of a monolayer of C101 dye adsorbed on a 6 μm thick opaque fiber TiO$_2$ film were measured using a UV−vis spectrophotometer (Varian Cary 5) equipped with an integrating sphere accessory (Figure 3). The absorptance (α) of the film, i.e., the fraction of incident light actually absorbed by the dye, is calculated from the relation $\alpha = 1 - R_d - T_d$. In the blue-green part of the spectrum ($\lambda = 400-550$ nm), absorptance was close to $\alpha = 0.8$ and peaked at $\alpha = 0.81$ at $\lambda_{max} = 550$ nm.

The photocurrent action spectrum of a DSC device made with the same film is shown in Figure 3. The incident photon to current conversion efficiency (IPCE) is given by IPCE(λ) = $[J(\lambda)/E_{in}(\lambda)]hc/(e\lambda)$, λ being the photon wavelength, h Planck's constant, c the speed of light, e the elementary charge, and $J(\lambda)$ the photocurrent density measured under monochromatic illumination at λ with an irradiance $E_{in}(\lambda)$. This spectrum is clearly far from saturation and peaks at a value of IPCE = 0.77 at $\lambda = 550$ nm. From these data, it is inferred that nanostructured fibers solar cells using 6 μm thick films, C101 dye sensitizer, and a volatile solvent-based electrolyte are characterized by a conversion quantum yield (absorbed photon-to-current conversion efficiency, APCE), given by APCE = IPCE/α, exceeding 90% in the spectral region between 550 and 650 nm. This nearly quantitative conversion yield indicates that adverse recombination processes taking place in the device are actually minimal.
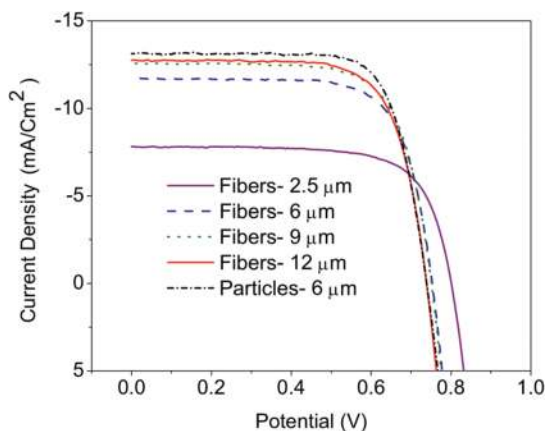
1634   DOI: 10.1021/nl904125q | Nano Lett. 2010, 10, 1632--1638

FIGURE 4. J–V characteristics of dye-sensitized solar cells based on fibrous photoanodes of various thicknesses.

TABLE 1. Photovoltaic Parameters of Dye-Sensitized Fiber- and Spherical Nanoparticle-Based Solar Cells with Various Film Thicknesses

anode type	thickness (μm)	V_{OC} (mV)	J_{SC} (mA/cm^2)	FF	efficiency (%)
fibers	2.5	801	7.81	0.72	4.50
	6	760	11.63	0.73	6.47
	9	760	13.0	0.72	7.15
	12	746	13.2	0.73	7.13
particles	6	739	13.1	0.74	7.27

Figure 4 shows the photocurrent density–voltage (J–V) characteristics of DSCs prepared with TiO$_2$ fibrous photoanodes of various thicknesses under simulated air mass 1.5 global (AM 1.5G) full sunlight intensity. The setup and method used for such measurements have been previously described.[5] Detailed photovoltaic parameters, namely, the open-circuit voltage (V_{OC}), short-circuit current density (J_{SC}), fill factor (FF), and the photovoltaic power conversion efficiency (η) are gathered in Table 1. Comparing devices containing nanostructured fiber-based photoanodes of increasing thickness, the open-circuit voltage V_{OC} of the DSCs was observed to be reduced as the thickness of the photoactive layer increases. This effect has been generally observed for DSCs based on nanotubes and nanoparticles.[14,19] It is due to the enhancement of the dark current, which results from the reduction of the electrolyte by conduction band electrons of TiO$_2$. An increase of the film thickness increases the solid–electrolyte contact surface area and hence proportionally the dark current. The excellent fill factor of the J–V characteristic for fibrous TiO$_2$ is quite comparable to the nanoparticulate morphology and does not suffer from the problem generally observed with nanotubes produced by anodization of a metal substrate. A photovoltaic power conversion efficiency of $\eta = 4.5\%$ was achieved with films only 2.5 μm thick. The highest efficiency of $\eta = 7.15\%$ was obtained with films of 9 μm thickness.

At similar film thickness ($d = 6$ μm), J_{SC} of nanoparticles-based devices was clearly higher by ca. 1.5 mA/cm^2 than that of the fiber-based cells, whereas V_{OC} was lower by 21

mV. The reduced current density obtained with fibers can be explained in terms of insufficient light harvesting by dye-sensitized films presenting a lower roughness factor and then lower optical absorbance. The higher V_{OC} has the same cause, as a decreased TiO$_2$ surface area minimizes the dark current.

The performance of a solar cell device is dependent on the kinetic competition between the electron back transfer from the conduction band of TiO$_2$ (e$^-_{cb}$) to the oxidized dye species (S$^+$) adsorbed on the surface (e$^-_{cb}$ + S$^+$ → S, rate constant k_b) and the dye regeneration process by the iodide-based electrolyte (S$^+$ + 2 I$^-$ → S + I$_2^-$, rate constant k_r). Earlier studies performed with nanoparticulate mesoporous TiO$_2$ layers concluded that e$^-_{cb}$–S$^+$ recombination is controlled to a large extent by trapping and detrapping of electrons at the surface of the oxide and at grain boundaries between spherical particles.[5,6] In the fibrous morphology, the number of contact points between long fibers, and therefore the number of traps, is expected to be considerably lower than between particles in mesoscopic layers. While k_r is expected to be comparable for both particle- and fiber-based cells, it is then likely that k_b is increased for nanostructured fibers films. Nanosecond transient diffuse reflectance spectroscopy was applied to dye-sensitized, opaque TiO$_2$ fiber layers to study the dynamics of parallel recombination and dye-regeneration reactions. Pulsed excitation (λ = 500 nm, 5 ns fwhm pulse duration, 200 μJ/cm^2 pulse energy fluence, 30 Hz repetition rate) was provided by an optical parametric oscillator (OPO, GWU OPO-355) pumped by a frequency-tripled, Q-switched Nd:YAG laser (Continuum, Powerlite 7030). The laser beam output was expanded by a plano-concave lens to irradiate a large cross section of the sample, whose surface was kept at a 30° angle to the excitation beam. The probe light, produced by a continuous wave Xe arc lamp, passed through a first monochromator tuned at $\lambda = 630$ nm and various optics and was focused onto the sample by the first 6:1, 90° off-axis ellipsoidal mirror of a modified *Praying Mantis* (Harrick) diffuse reflection accessory. Diffuse reflected light was collected by the second ellipsoidal mirror, intercepting ca. 20% of the total reflection at all angles between 0 and 90° from the surface and was directed to a second monochromator before being detected by a fast photomultiplier tube. Data waves were recorded on a DSA 602A digital signal analyzer (Tektronix). Satisfactory signal-to-noise ratios were typically obtained by averaging over 3000 laser shots.

Assuming the sample was optically thick, diffuse reflectance changes ΔR_d can be treated using Kubelka–Munk function[20]

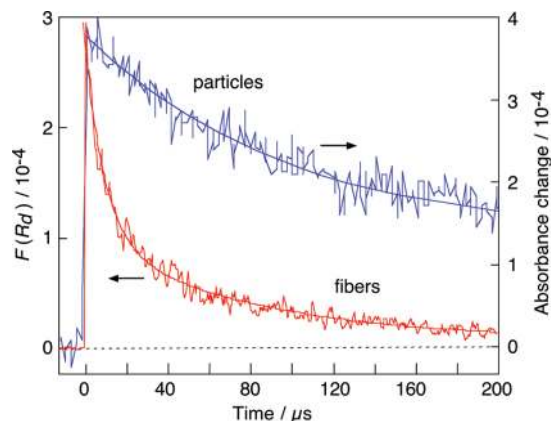$$F(\Delta R_d) = \frac{(1 - \Delta R_d)^2}{2\Delta R_d} \propto \varepsilon_M C_M \qquad (1)$$

FIGURE 5. Temporal behavior of the Kubelka—Munk function $F(\Delta R_d)$ of the transient diffuse reflectance measured at $\lambda = 630$ nm for a C101 dye-sensitized, 6 μm thick, TiO$_2$ fibrous opaque film covered by a redox-inactive ionic liquid upon nanosecond pulsed laser excitation. A typical transient absorbance decay curve obtained in identical conditions with a 8 μm thick, dye-sensitized transparent mesoporous TiO$_2$ layer made of 20 nm diameter spherical particles is shown for comparison.

FIGURE 6. Open circuit voltage at different charge density levels for dye-sensitized cells made of TiO$_2$ nanoparticles or fibers.

where ΔR_d is the reflectance change of the sampled layer, ε_M the molar decadic extinction coefficient of the absorber, and C_M its molar concentration in the film volume. Figure 5 shows the transient decay of $F(\Delta R_d)$ recorded at $\lambda = 630$ nm for a C101 dye-sensitized, 6 μm thick, opaque TiO$_2$ fiber film covered by a thin film of the redox-inactive ionic liquid 3-methyl-1-ethylimidazolium bis(trifluoromethane)sulfonimide (EMITFSI). The $F(\Delta R_d)$ function (eq 1) is proportional to the concentration of the oxidized state S$^+$ of dye sensitizer following ultrafast photoinduced electron injection from the excited dye into the conduction band of TiO$_2$. In the absence of a redox electrolyte, the decrease of the signal reflects the dynamics of the recombination of conduction band electrons with the oxidized dye S$^+$. In such conditions, a half reaction time $t_{1/2} = 18$ μs was measured.

The observed recombination rate is 1 order of magnitude faster than that in typical mesoporous systems made of sintered spherical particles sensitized by C101 in similar conditions ($t_{1/2} = 180$ μs). This striking difference indicates that indeed electrons injected in TiO$_2$ nanostructured microfibers experience less trapping than in sintered particles. Rather than being restricted to the volume of one nanocrystalline particle, where they stay in the vicinity of a single oxidized dye molecule, electrons in fibers can also rapidly move to other injection sites, giving rise to a second-order rate kinetics for the recombination reaction and resulting in a marked decrease of $t_{1/2}$.

Transient photovoltage measurements were performed to monitor the electron transport dynamics in TiO$_2$ fiber films and to compare it with the behavior of electrons in nanoparticulate films. The method relied on measuring the temporal response of transient open circuit photovoltage upon excitation of the DSCs by a short, low-amplitude red light pulse, superimposed on a steady-state white light irradiation bias.[21,22] Various intensities of the light bias were
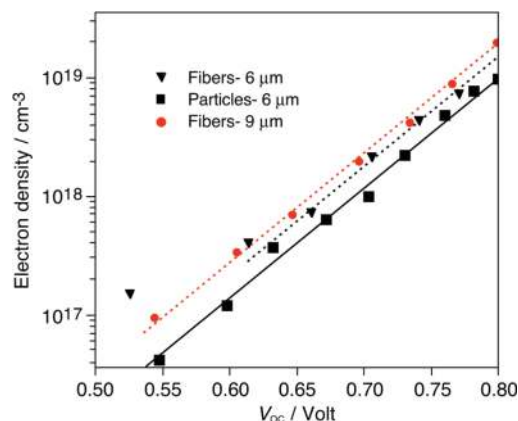
generated by a white light emitting diode array. Red light pulsed diodes (square wave, 100 ns rise and fall times, 50 ms pulse duration) controlled by a fast solid-state switch were used as the perturbation source. The voltage dynamics were recorded on a PC-interfaced Keithley 2400 source meter. The pulsed red light intensity was set to a low level to keep the modulated photovoltages values below 10 mV. In such conditions the voltage decay dynamics remained monoexponential. When the white light bias intensity is varied, the lifetime τ_{rec} characterizing the rate of interfacial charge recombination between conduction band electrons in the TiO$_2$ and the oxidized mediator species I$_3^-$ in the electrolyte could be estimated from the decay dynamics over a range of biased V_{OC} values. Besides, the electron transport lifetime τ_n within the oxide network to the back contact was obtained by recording the rise time of the perturbed open circuit photovoltage.[21,22] Between each point and before the white LEDs switched to the next intensity, a charge extraction routine was executed by rapidly short circuiting the cell.

The photoinduced electron density in the TiO$_2$ film imposed by the light bias at open circuit, n (cm^{-3}), was estimated from transient photocurrent measurements using the same setup.[23] The electron density was determined as $n = \Delta Q/[ed(1 - p)]$, where e is the elementary charge, d the film thickness, and p the porosity of the oxide material. ΔQ is the extra charge injected per irradiated surface area during the pulsed excitation. The value of ΔQ was determined experimentally by integrating the photocurrent density temporal decay at short circuit condition. The density of injected electrons measured at various bias light intensities, is plotted against the corresponding values of the V_{OC} in Figure 6. The V_{OC} of fiber DSCs at constant photoelectron density is observed to be 20−30 mV lower than for nanoparticle DSCs. The value of n is indicative of the energy difference between the conduction band edge and the electron quasi-Fermi level under illumination. A lower V_{OC} at a given value of the photoelectron density can only be attributed to downward movement of the conduction band edge energy.[24] Since the electrolyte used in both types of
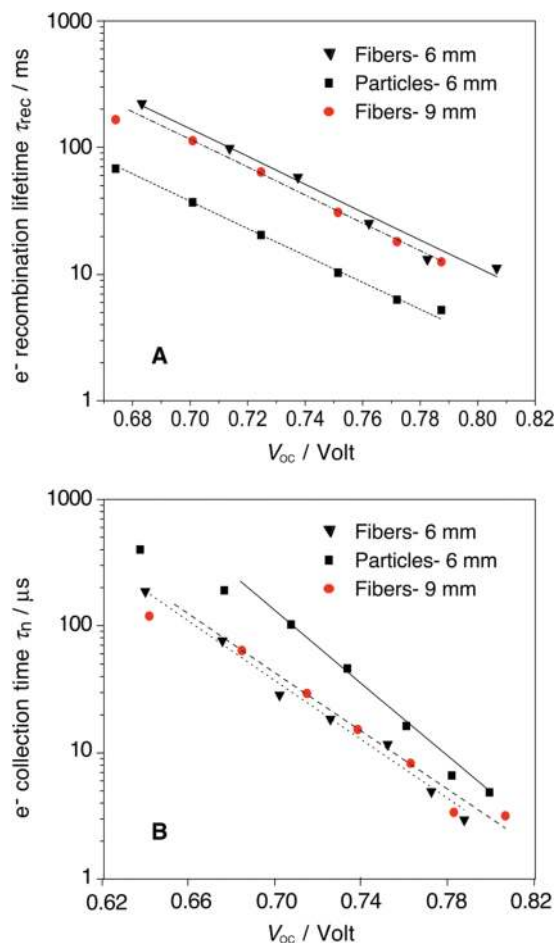
FIGURE 7. (A) Electron recombination lifetime τ_{rec} and (B) electron collection time τ_n extracted respectively from transient open circuit photovoltage decay and rise measurements in fiber- and spherical nanoparticle-based DSCs.

DSCs was identical, the small shift of the conduction band of TiO$_2$ to more positive potentials apparent in fibrous potoanodes can probably be explained by the absence of contamination by Cl$^-$ ions that generally characterize nanoparticles prepared from TiCl$_4$ precursor. A somehow lower loading density of the TiO$_2$ surface by the anionic dye C101 is also likely to contribute to the same effect.

Figure 7 compares recombination (τ_{rec}) and transport (τ_n) lifetimes of electrons in TiO$_2$ fiber- and nanoparticle-based DSCs at various light-biased open circuit potentials V_{OC}. A potential shift of 40−50 mV was observed between points at comparable τ_{rec} values measured in fibrous systems compared to the particulate ones. This V_{OC} shift is clearly larger than that obtained at constant photoinduced electron density (Figure 6). Thus, for a common film thickness of 6 μm, nanostructured fiber-based photoanodes exhibited τ_{rec} values about 3 times larger than for nanoparticles at a same charge density. Trapping of carriers was observed from the laser experiments to be reduced in the oxide fibers material and electron transfer rate to the dye oxidized state was apparently accelerated compared to the nanoparticulate

situation. Here, however, interfacial charge transfer to the electrolyte is markedly slowed down. This effect is ascribed to the particular morphology of pores surrounding the oxide fibers. Rather than being confined in mesoscopic cavities between nanocrystalline particles, triiodide ions have the possibility to escape faster and farer and to diffuse more freely to the counter electrode. Figure 7b compares the electron collection time τ_n for the two morphologies. Here again, titania fibers appear clearly superior, as they transport electrons to the back contact approximately 2−3 times faster than particles networks. Interestingly, no difference is observed between fibrous photoanodes of 6 and 9 μm thickness. This tends to indicate that ca. 10 μm long fibers can in both cases transport electrons toward the back contact with a comparable efficiency. J−V curves of Figure 4 show that the unfavorable downward conduction band edge movement is compensated by the slower recombination and that the combined effect of both phenomena corresponds to a net improvement in V_{OC} of the fibrous DSCs of about 21 mV at constant light intensity.

In conclusion, highly porous photoanodes made of unoriented TiO$_2$ nanostructured hollow fibers show remarkably enhanced electron transport properties compared to mesoporous films made of spherical nanoparticles. The retardation of surface recombination between conduction band electrons and I$_3^-$ species in the electrolyte observed in nanostructured fiber-based cells is able to offset the adverse shift of the band edge toward positive potential and produce a net open-circuit photovoltage gain of about 21 mV. Although still suffering from lower roughness factor and decreased ability to harvest incident light, TiO$_2$ fibers offer obvious advantages that should inspire new developments in the design of improved heterojunction structures in DSC and HOPV applications. The reduced number of contact points between sintered units, which are believed to constitute the main trapping sites for conduction band electrons, as well as the open morphology of pores around the fibers, allowing for a fast diffusion of the electrolyte, are key to the excellent performances achieved with this cheap material. The advent of new stable organic dye sensitizers characterized by higher extinction coefficients[25] enables sufficient light harvesting with reduced dye loading and, therefore, eases the requirement for a large roughness factor. Further efforts aiming at decreasing the diameter of the fibers and thus increasing the roughness factor of fibrous photoanodes are currently pursued. Application of TiO$_2$ nanostructured hollow fibers in DSCs based on ionic liquids will also be studied. Such solvent-free systems are indeed quite beneficial in terms of stability at high working temperature. The viscosity of the electrolyte in conventional mesoporous cells imposes a limitation to the mass transport at strong light intensity. Photoanodes made of fibrous material characterized by a much lower tortuosity of the pores are then expected to bring a decisive advantage when viscous electrolytes are used.

NANO LETTERS

REFERENCES AND NOTES

(1) O'Regan, B.; Grätzel, M. *Nature* **1991**, *353*, 737–740.
(2) Grätzel, M. *Nature* **2001**, *414*, 338–344.
(3) Ito, S.; Chen, P.; Comte, P.; Nazeeruddin, M. K.; Liska, P.; Péchy, P.; Grätzel, M. *Prog. Photovoltaics* **2007**, *15*, 603–612.
(4) Gao, F.; Wang, Y.; Shi, D.; Zhang, J.; Wang, M.; Jing, X.; Humphry-Baker, R.; Wang, P.; Zakeeruddin, S. M.; Grätzel, M. *J. Am. Chem. Soc.* **2008**, *130*, 10720–10728.
(5) Haque, S. A.; Tachibana, Y; Willis, R. L.; Moser, J. E.; Grätzel, M.; Klug, D. R.; Durrant, J. R. *J. Phys.Chem. B* **2000**, *104*, 538–547.
(6) Nelson, J.; Chandler, R. E. *Coord. Chem. Rev.* **2004**, *248*, 1181–1194. (c) Nelson, *J. Phys. Rev. B* **1999**, *59*, 15374–15380.
(7) Wang, Q.; Moser, J. E.; Grätzel, M *J. Phys. Chem. B* **2005**, *109*, 14945–14953.
(8) Song, M. Y.; Kim, D. K.; Ihn, K. J.; Jo, S. M.; Kim, D. Y. *Nanotechnology* **2004**, *15*, 1861–1865.
(9) Fujihara, K.; Kumar, A.; Jose, R.; Ramakrisna, S.; Uchida, S. *Nanotechnology* **2007**, *18*, 365709.
(10) Chuangchote, S.; Sagawa, T.; Yoshigawa, S. *Appl. Phys. Lett.* **2008**, *93*, No. 033310.
(11) Jose, R.; Kumar, A.; Thavasi, V.; Ramakrishna, S. *Nanotechnology* **2008**, *19*, 424004–424011.
(12) Mukherjee, K.; Teng, T. H.; Jose, R.; Ramakrisna, S. *Appl. Phys. Lett.* **2009**, *95*, No. 012101.
(13) Enach-Pommer, E.; Liu, B.; Aydil, E. S. *Phys. Chem. Chem. Phys.* **2009**, *11*, 9648–9652.
(14) Kuang, D.; Brillet, J.; Chen, P.; Takata, M.; Uchida, S.; Miura, H.; Sumioka, K.; Zakeeruddin, S. M.; Grätzel, M. *ACS Nano* **2008**, *2*, 1113–1116.
(15) Zhu, K.; Neale, N. R.; Miedaner, A.; Frank, A. J. *Nano Lett.* **2007**, *7*, 69–74.
(16) Mor, G. K.; Shankar, K.; Paulose, M.; Varghese, O. K.; Grimes, C. A. *Nano Lett.* **2006**, *6*, 215–218.
(17) Feng, X.; Shankar, K.; Varghese, O. K.; Paulose, M.; Latempa, T. J.; Grimes, C. A. *Nano Lett.* **2008**, *8*, 3781–3786.
(18) Varghese, O. K.; Paulose, M.; Grimes, C. A. *Nat. Nanotechnol.* **2009**, *4*, 592–597.
(19) Kuang, D. B.; Ito, S.; Wenger, B.; Klein, C.; Moser, J. E.; Humphry-Baker, R.; Zakeeruddin, S. M.; Grätzel, M. *J. Am. Chem. Soc.* **2006**, *128*, 4146–4154.
(20) Kubelka, P.; Munk, Z. *Z. Tech. Phys.* **1931**, *12*, 593–601.
(21) O'Regan, B. C.; Durrant, J. R. *J. Phys. Chem. B* **2006**, *110*, 8544–8547.
(22) Barnes, P. R. F.; Liu, L.; Li, X.; Anderson, A. Y.; Kisserwan, H.; Ghaddar, T. H.; Durrant, J. R.; O'Regan, B. C. *Nano Lett.* **2009**, *9*, 3532–3538.
(23) Zhang, Z.; Zakeeruddin, S. M.; O'Regan, B. C.; Humphry-Baker, R.; Grätzel, M. *J. Phys. Chem. B* **2005**, *109*, 21818–21824.
(24) Kopidakis, N.; Neale, N. R.; Frank, A. J. *J. Phys. Chem. B* **2006**, *110*, 12485–12489.
(25) Grätzel, M. *Acc. Chem. Res.* **2009**, *42*, 1788–1798.